The use of a semi-structured finite-element mesh in 3-D resistivity inversion

M.H. Loke[1*], P.B. Wilkinson[2], O. Kuras[2], P.I. Meldrum[2] and D.F. Rucker[3]

[1] Geotomo Software Sdn Bhd (Malaysia), 115 Cangkat Minden Jalan 5, 11700 Gelugor,

Penang, Malaysia

Email : drmhloke@yahoo.com, [*] Corresponding author

[2] British Geological Survey, Keyworth, Nottingham, NG12 5GG, U.K.

emails : pbw@bgs.ac.uk, oku@bgs.ac.uk, pime@bgs.ac.uk

[3] hydroGEOPHYSICS Inc., 2302 North Forbes Boulevard, Tucson, AZ 85745, U.S.A.

email : druck8240@gmail.com

Short running title : Semi-structured mesh in 3-D resistivity inversion

Keywords : Resistivity, Modelling, Numerical study, Inversion, Tomography

Data Availability Statement

The data that support the findings of this study are available from the corresponding author upon reasonable request.

Abstract

Calculating the electric potentials for 3-D resistivity inversion algorithms can be time consuming depending on the structure of the mesh. There have been generally two approaches to generating finite-element meshes. One approach uses a structured rectangular mesh with hexahedral elements on a rectangular model grid. The distribution of the model cells can be designed to follow known boundaries, and directional roughness constraints can be easily imposed. A 1-D wavelet transform that takes advantage of the regular arrangement of the model cells can also be used to reduce the computer time and memory required to solve the smoothness-constrained least-squares equation. However, the structured rectangular mesh uses an unnecessarily fine mesh in parts of the model that are far away from the electrodes where the potential changes gradually. A second approach uses an unstructured mesh with tetrahedral elements created automatically by a mesh generation program with finer elements nearer the electrodes and coarser elements in the more remote regions. This generates a mesh with a much smaller number of nodes. The disadvantage is that an irregular model grid is normally used. We examine an alternative approach that combines structured and unstructured meshes. We employ a regular model grid with a finer mesh near the surface and a coarser mesh in deeper regions using a combination of hexahedral and tetrahedral elements. The semi-structured mesh reduces the calculation time by more than three times compared to a structured mesh. An adaptive semi-structured mesh that also uses a coarser mesh for model cells near the surface if they are more than one unit electrode spacing from the nearest electrode was also developed for surveys with non-uniform data coverage. For the Bonsall Leys field survey, that used a capacitively coupled mobile system and collected a data set with nearly a million electrode positions, the adaptive mesh reduces the calculation time by about 80%. The calculation time can be further reduced by about 93% when it is combined with a mesh segmentation method.

Introduction

In recent years, 3-D electrical resistivity tomography (ERT) surveys have been more widely adopted to map the subsurface in regions with complex geology (Loke *et al.*, 2013). Advances in field instrumentation and automatic inversion software allow the execution of large 3-D surveys. Most surveys use electrodes on the ground surface, creating very large data sets with hundreds of thousands of data points and electrode positions incorporating multichannel resistivity meters, particularly with mobile systems (Simyrdanis *et al.*, 2015; Unrau, 2019; Loke *et al.*, 2020). The inverse model can have hundreds of thousands of cells and the processing of such large data sets within a reasonable time is a challenging task with PCs.

The finite-element method (FEM) is widely used to calculate the potentials for the inverse model within an automatic inversion program as it can easily model the surface topography (Holcombe and Jiracek, 1984; Loke, 2000). Two common approaches have been used to construct the finite-element mesh. One approach uses a trapezoidal (for 2-D models) or hexahedral (for 3-D models) mesh elements. The nodes are arranged in a simple rectangular pattern if there is no topography. The regular pattern of nodes is simple to implement and widely used in earlier work (e.g., Loke and Barker, 1996a;b). In some areas, the geological units have a layered structure. The model can be adjusted to more closely match the known boundaries. The roughness filters that constrain the model can be easily modified to emphasise structures with a known orientation, such as horizontal or sloping boundaries (Farquharson, 2008). For example, in a predominantly layered environment, the roughness filter in the horizontal directions can be given a larger weight than in the vertical direction. The disadvantage is that an unnecessarily fine mesh is used in parts of the model that are far away from the electrodes where the potential changes gradually.

A more recent approach uses an unstructured mesh with triangular or tetrahedral elements (Günther *et al.*, 2006) which are created by an automatic mesh generation program such as Tetgen (Si, 2020). The regions near the electrodes require a finer mesh, but remote regions far from the electrodes can adopt a coarser mesh. This generates a mesh with a much smaller number of nodes which can significantly reduce the calculation time. However, the irregular grid makes it more difficult to impose directional constraints or to use the 1-D wavelet transform to reduce the Jacobian matrix size (Loke *et al.*, 2020) in the inversion algorithm. In this paper, we propose an alternative semi-structured mesh that attempts to combine the advantages of both methods while minimising their disadvantages. A model grid with the cells arranged in a rectangular pattern is used together with a combination of trapezoidal and triangular (for 2-D models) or hexahedral and tetrahedral (for 3-D models) mesh elements to reduce the number of nodes in the finite-element mesh. The reduced number of nodes in our hybrid approach has the distinct advantage of faster computation and lower memory requirements while keeping the numerical accuracy of traditional meshing methods.

It should be noted that significant progress had been made in devising directional roughness filters for a completely unstructured mesh (Lelièvre and Farquharson, 2013). However, the rectangular model grid system has the advantage that it is easier to apply the wavelet compression method to reduce the size of the Jacobian matrix, which is essential for very large data sets and models.

Similar techniques to reduce the number of nodes in the mesh have been developed for EM surveys based on the finite-difference method (Haber and Heldmann, 2007; Cherevatova *et al.*, 2018). The multi-resolution technique was adapted by Gao *et al.* (2020) for resistivity modelling. However, many ERT surveys are conducted in areas with significant topography, and the finite-difference method is less efficient in modelling topography compared to the finite-element method used in this paper.

The following section gives the theoretical background for the least-squares inversion method followed by a description of mesh elements used by the FEM and how they are used by the proposed semi-structured methods. Following the background section, we compare inversion results using a structured rectangular mesh and the semi-structured meshes for a synthetic model and a field data set.

Method

Smoothness-constrained least-squares inversion method

A typical equation used widely in 2-D and 3-D resistivity inversion by the smoothness-constrained least-squares optimisation method gives the relationship between the model parameters and the measured data (deGroot-Hedlin and Constable, 1990; Loke *et al.*, 2013):

$$\left[\mathbf{J}_i^T \mathbf{R}_d \mathbf{J}_i + \lambda_i \mathbf{W}^T \mathbf{R}_m \mathbf{W}\right] \Delta \mathbf{r}_i = \mathbf{J}_i^T \mathbf{R}_d \mathbf{g}_i - \lambda_i \mathbf{W}^T \mathbf{R}_m \mathbf{W} \left(\mathbf{r}_{i-1} - \mathbf{r}_m\right). \tag{1}$$

In our work, we logarithmically transform both the model parameter and the data parameter, which represents the calculated model resistivity and measured apparent resistivity, respectively (Johansen, 1977). $\mathbf{r}$ is the model parameter vector while $\mathbf{g}$ is data misfit vector. $\Delta \mathbf{r_i}$ is the change in the model parameters to reduce the data misfit $\mathbf{g}$ which is calculated by solving equation (1). $\mathbf{r_{i-1}}$ is the model from the previous iteration and $\mathbf{r}_m$ is a reference model. The Jacobian matrix $\mathbf{J}$ contains the partial derivatives of the model response with respect to the model parameters. $\mathbf{W}$ is the roughness filter (deGroot-Hedlin and Constable, 1990) and λ is the damping factor (Farquharson and Oldenburg, 2004). $\mathbf{R_d}$ and $\mathbf{R_m}$ are data and model weighting matrices used for the L1-norm inversion method (Farquharson and Oldenburg, 1998). The iterative linear-conjugate gradient method (Press *et al.*, 2007) is used to solve the least-squares equation.

Finite-element forward modelling method

The finite-element method (FEM) is used in this paper as many ERT surveys are carried out in areas with significant topography (Günther *et al.* 2006; Udphuay *et al.*, 2011; Loke *et al.*, 2022a). The method of discretization within the FEM allows for greater flexibility to model complex topography accurately by using a deformed hexahedral or tetrahedral mesh (Loke, 2000) where the nodes on the surface match the observed ground surface elevation. In comparison, the finite-difference method is normally restricted to rectangular mesh elements which would require a very fine upper mesh to accurately model areas with large elevation changes (Gao *et al.*, 2020), significantly increasing the total number of nodes. Within the inverse model, the finite-element capacitance matrix equation is solved to calculate the potential at each node (Loke *et al.*, 2020). Figure 1a shows the mesh for a 2-D model using rectangular elements as an example. Most surveys use electrodes planted on the ground surface. Since the electric potentials vary greatly near the current electrodes, sufficiently accurate results require a finer mesh nearer the electrodes, with at least four nodes between adjacent electrodes (Dey and Morrison, 1979). The limitation of the rectangular mesh is that the same fine mesh is used in the deeper levels where the potentials vary gradually. Figure 1b shows a semi-structured mesh (Loke *et al.*, 2021) with a coarser mesh at the deeper levels using triangular elements to connect levels with different number of nodes. For most data sets, the semi-structured 2-D mesh reduces the number of nodes by about half and the calculation time by about four times. The time taken by FEM is usually not a problem for 2-D inverse problems as the least-squares method usually converges in less than ten iterations and within minutes even with a dense mesh. However, for global optimisation methods that require tens to hundreds of thousands of iterations (Aleardi *et al.*, 2021), the reduction in the calculation time required by the FEM can be a significant factor.

Triangles are the simplest elements for 2-D models (tetrahedral elements for 3-D models) and have several advantages. The Dirichlet matrix with simplex coordinates for the triangular element has a simple form which is independent of the true coordinates at the vertices of the triangle (Silvester and Ferrari, 1990). Any structure can be decomposed into triangular elements, making the use of triangular elements (and tetrahedral elements in 3-D meshes) attractive. Figure 1c shows the decomposition of a rectangular element into two triangular sub-elements. One small disadvantage of a triangular element is that it is a non-symmetrical element. If a rectangular mesh (Figure 1a) is decomposed into triangular elements, the calculated apparent resistivity values when plotted in a pseudosection for a symmetrical array (such as the Wenner and dipole-dipole) over a symmetrical structure will be non-symmetrical. To eliminate the asymmetry, we calculate the coupling coefficients between the nodes using two opposite subdivisons of the rectangle (Figure 1c), and use the average of the coupling coefficient values. A 3-D hexahedral element can be subdivided into five tetrahedral sub-elements (Pridmore *et al.*, 1981; Silvester and Ferrari, 1990). In a similar way, we can avoid the asymmetry by subdividing the hexahedral element in two opposite directions and use the average of the coupling coefficients. The symmetrical coupling coefficients from the average of two opposite subdivisions of a hexahedral element into tetrahedral elements are used in this paper.

We calculate the FEM potentials by solving the following capacitance matrix equation (Sasaki, 1989; Silvester and Ferrari, 1990; Loke *et al.*, 2020).

$$\mathbf{C}\boldsymbol{\Phi} = \mathbf{s} \tag{2}$$

$\boldsymbol{\Phi}$ is a vector that contains the potentials at the nodes of the finite-element mesh while $\mathbf{s}$ is the current source vector. $\mathbf{C}$ is the capacitance matrix that contains the coupling coefficients between the nodes in the mesh. $\mathbf{C}$ is a very sparse n by n matrix, where n is the number of nodes in the mesh. The $\mathbf{C}$ matrix is assembled by adding the coupling coefficients between the

nodes for all the elements in the mesh. Details on calculating the coupling coefficients for different types of 2-D and 3-D elements can be found in Silvester and Ferrari (1990). The computer memory and time required to solve the capacitance matrix equation is proportional to the number of nodes in the mesh.
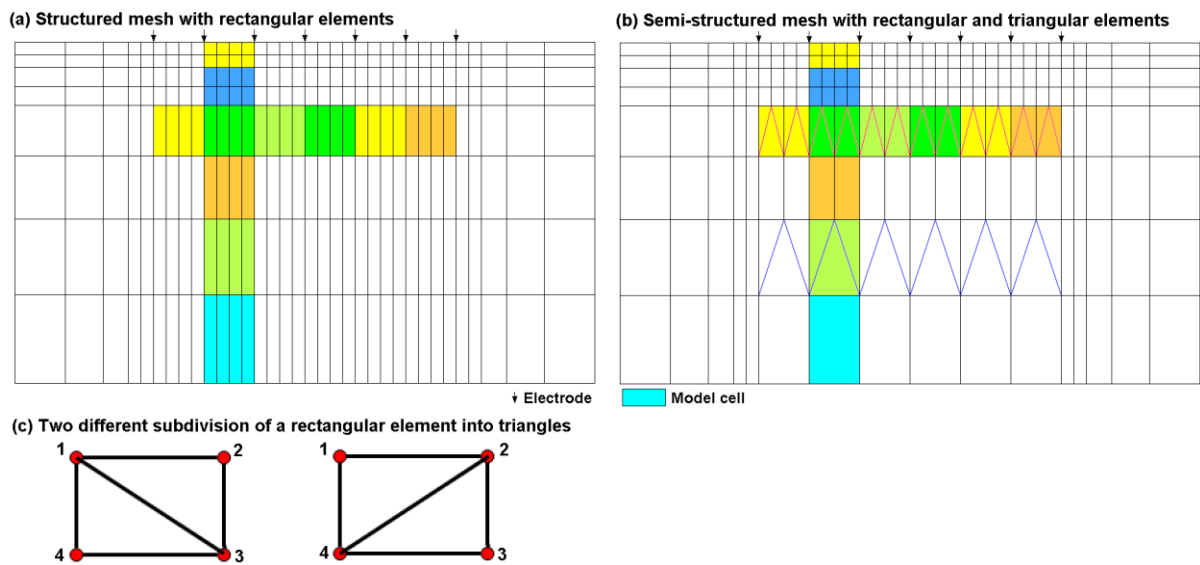

Figure 1 (a) A structured rectangular 2-D mesh (vertical cross-section) with four nodes between adjacent electrodes. (b) A semi-structured mesh with four nodes for mesh levels near the surface and one node for deeper levels. (c) Two possible subdivisions of a rectangular element into triangular sub-elements.

A similar scheme using a combination of quadrilaterals and triangles for 2-D grids was proposed by Hermann *et al.* (2011). However, the scheme was non-conformal in that some faces at the interface between regions with different node densities might not share the same nodes at their vertices (Lelièvre and Farquharson, 2013). It should be noted that the multi-resolution (Gao *et al.*, 2020) and octree (Xiao *et al.*, 2022) methods also have 'hanging nodes' at the interface between two regions with different node densities. The nodes at the interfaces in the semi-structured mesh are shared by all adjacent elements (i.e. it is conformal) which

ensures the potentials at the nodes are continuous across different types of elements. The semi-structured mesh method can be viewed as a conformal version of the octree and multi-resolution methods which removes the need for special interpolation functions for 'hanging nodes' by using the finite-element method.

The 3-D semi-structured mesh method

This section describes in more detail the semi-structured mesh technique introduced by Loke *et al.* (2021). Figure 2a shows three mesh levels in a 3-D structured rectangular mesh at different depths. The nodes are located at the intersections of mesh lines. The same arrangement of the nodes is used for all the mesh levels in the 3-D finite-element mesh. The structured rectangular mesh only uses hexahedral elements and pink lines (Figure 2) represent the model grid. Four mesh lines subdivide each model cell in both x and y directions. A number of buffer mesh lines are used around the central region so that the boundaries of the mesh are sufficiently far away from the central region where the model grid and electrodes are located. Figure 2b shows the mesh used by the semi-structured mesh at a few mesh levels. At the topmost five mesh levels, in the central region where the survey electrodes are located, four mesh lines subdivide each model cell in both x and y directions. Below the top five mesh levels, only two mesh lines subdivide the model cells in the x and y directions, which is futher reduced to one mesh line below the seventh mesh level. Hexahedral elements are used in most of the mesh, and tetrahedral elements are used in the transition zones to connect regions with different node densities. For large rectangular meshes with more than a million nodes, the semi-structured mesh reduces the number of nodes and calculation time by about three to four times. One advantage of using a structured model grid compared to a completely unstructured grid is that it is easier to tailor the arrangement of the cells and the roughness filters for different geological situations. Another advantage is that it is simpler to construct the Hilbert curve to

convert a 3-D Jacobian matrix into a 1-D function. This is followed by a fast 1-D wavelet compression (Davis and Li, 2013; Loke *et al.*, 2020) to reduce the computer memory and time required to solve the least-squares equation. Models containing data sets with hundreds of thousands of data points and an inverse model with a similar number of cells have a significant advantage when employing the compression method. The wavelet compression method can also reduce the size of the Jacobian matrix by about one hundred times. For very large data sets and models, the size of the full Jacobian matrix can exceed the computer memory, making wavelet compression essential.

Since the survey grid uses hexahedral elements near the electrodes, the problem of asymmetry in the calculated apparent resistivity values caused by using tetrahedral elements is reduced. The tetrahedral elements are located beyond the edges of the survey grid, or at the deeper mesh levels, which are further away from the electrodes on the surface. In the inverse model, we follow the approach by Maurer and Friedel (2006) where we extend the model grid slightly beyond the limits of the survey grid. The extended model grid reduces artefacts due to anomalies outside the survey grid. Loke *et al.* (2020) showed that model cells at three to four unit electrode spacings from the edge of the survey area still have significant model resolution values. Thus, we extend the edge of model grid by at least three unit spacings from the outermost electrodes used in the survey.

For the 2-D mesh, we use triangular elements to vertically connect mesh levels with different number of nodes (Figure 1b), such as between a mesh level with four nodes per model cell to a level below with two nodes. This makes the subdivision of the mesh into rectangular and triangular elements straightforward. The complexity increases for the 3-D mesh, as the transition between regions with different node densities occurs in both the horizontal and vertical directions. Figure 3a shows an example with six nodes on the front face (nodes 1-2-3-6-7-8) and four nodes on the back face (nodes 4-5-9-10) of a rectangular cell. In this case, the

rectangular cell has ten nodes (compared to eight nodes for a conventional rectangular element). For such a non-conventional arrangement of the nodes, we use the Tetgen program (Si, 2020) to subdivide the cell into nine tetrahedral elements. The groups of four nodes for each tetrahedral element are shown in Figure 3. We calculate the coupling coefficients for the nodes in the non-conventional rectangular cell with ten nodes by summing up the coupling coefficients of the tetrahedral elements within the cell. The subdivision is only done once and the node combinations for the tetrahedral elements are included in the computer program code. They are used for all the rectangular cells that have the same configuration, such as on the left, right, front and back transition zones. Altogether, we employ seven different types of non-conventional rectangular cells for the transition zones.

We note a similar scheme was used by (Gao *et al.*, 2020) for the finite-difference method with a finer mesh near the surface and a sparser mesh at deeper levels using an interpolation method to handle nodes between mesh levels with different node densities. In this paper we use the finite-element method which is more versatile in modelling topography by using tetrahedral elements to model mesh cells located between regions with different node densities. The use of tetrahedral elements also enables the use of sparser mesh cells on the same horizontal mesh level as described in the following section.

The 3-D adaptive semi-structured mesh method

The simple semi-structured mesh technique reduces the number of nodes within the model grid in the vertical direction but not in the horizontal direction. This is probably optimal where the electrodes are uniformly distributed within the survey grid such that most of the model cells are within one unit electrode spacing from an electrode. In some surveys, particularly using mobile systems, the data coverage is frequently non-uniform with significant areas that are not crossed by the survey tracks. For such areas, it is not necessary to use a fine

mesh for all the near surface model cells. We present a new 'adaptive' modification to the semi-structured mesh where model cells more than one unit spacing from the nearest electrode use a sparser mesh with two nodes in the horizontal direction for the near surface cells. This is reduced to one node for model cells that are more than two unit electrode spacings from the nearest electrode. The algorithm and the corresponding computer code turns out to be simpler. The steps used are as follows.

1. Determine the minimum distance of an edge of each model cell to the nearest electrode. Assign a node density of four for the cells that are within one unit spacing from an electrode, two nodes for cells that are between one and two unit spacings away, and finally one node for the remaining cells.

2. To create the mesh for a model cell, compare the node density of the cell with the adjacent cells. If the node density is greater or equal to the node density for all the neighboring cells, hexahedral elements are used. If the node density is less than any of the neighboring cells, the Tetgen (Si, 2020) subroutine is called by the computer code to automatically subdivide the model cell into tetrahedral elements.

As shown in Figure 2c, most of the cells are hexahedral while the tetrahedral cells are only used at the transition zones. Thus only a small number of calls to the Tetgen subroutine is needed that greately reduces the time needed to generate the mesh compared to a completely unstructured mesh. The algorithm operates in a similar way as a completely unstructured mesh in automatically allocating a dense mesh near the electrodes and a sparser mesh further away, except the model cells are hexahedral instead of tetrahedral in shape. It is possible to further reduce the total number of nodes by amalgamating several cells with one node towards the sides and bottom of the mesh into a single cell. However, in most cases, this will reduce the total number of nodes by less than five percent. This will greatly increase the complexity of

the computer program but will not significantly reduce the computer time and memory required to invert the data set.
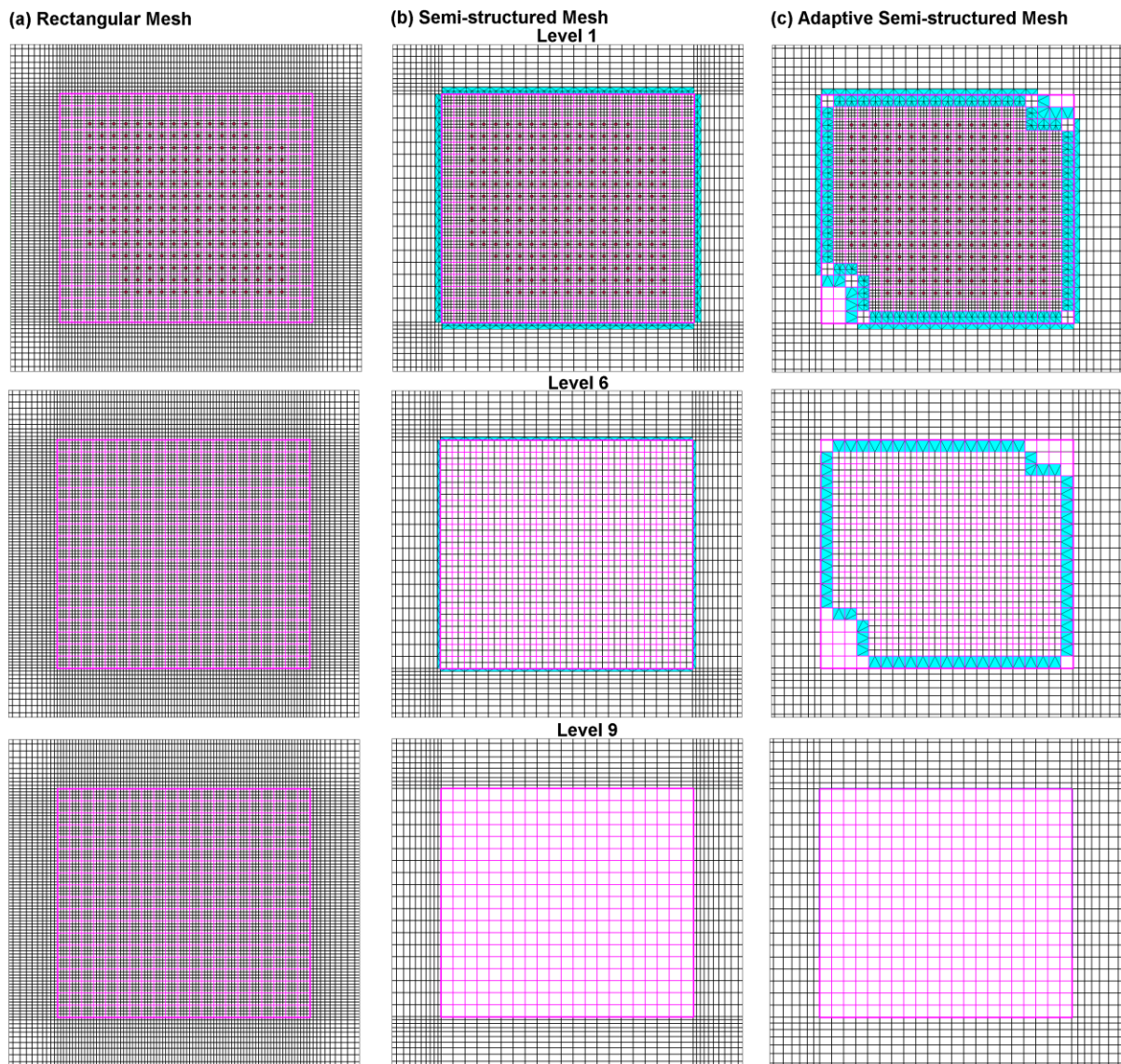

Figure 2 (a) Plan view of rectangular mesh at three different mesh levels. (b) Semi-structured mesh with four nodes for each model cell in top four levels, two nodes in intermediate levels and one node for lower levels. (c) Adaptive semi-structured mesh with two nodes for model cells between one and two unit electrode spacings from the nearest electrode and one node for cells further away at the top mesh levels. The hexahedral elements are coloured white while the tetrahedral elements are light blue. The outline of the model grid is marked by the thick pink line. The electrodes are marked by small red circles in the top mesh level.
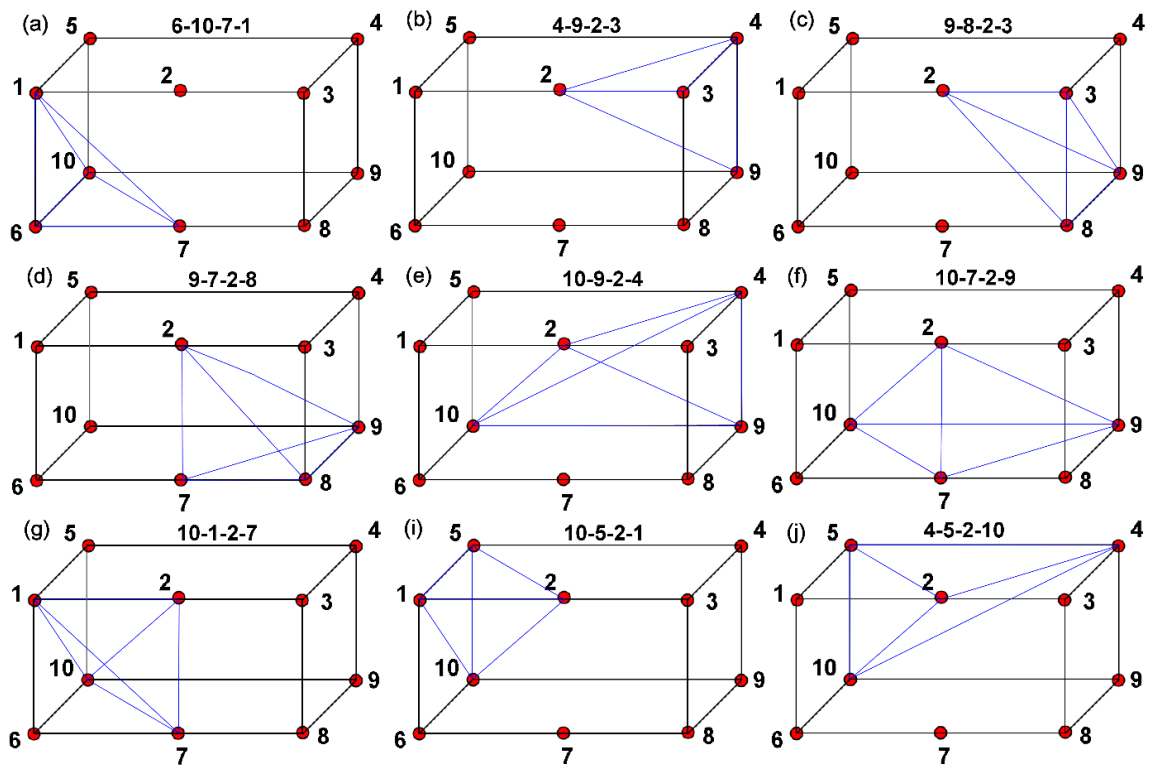
Figure 3 Subdivision of a rectangular cell with six nodes on the front vertical face and four nodes on the back vertical face into tetrahedral elements. The local node numbers for each tetrahedral element are listed above the hexahedral element outline.

Solving the FEM capacitance matrix equation

The capacitance matrix equation (2) must be solved in order to determine the potentials at the nodes of the mesh. There are two main classes of the methods to solve the matrix equation, iterative and direct methods (George and Liu, 1981; Press *et al.*, 2007). Oldenburg *et al.* (2013) made a comparison of iterative and direct methods for solving the capacitance matrix equation for large 3-D EM forward models with many sources. It was found that for a small number (less than10) of sources iterative methods are faster than direct methods, but for a large number of sources direct methods are faster. As an example, for a model with a mesh of 343,000 nodes and 1,000 sources, the direct method was found to be about 300 times faster

than the iterative method (Oldenburg *et al.*, 2013). Tests carried out with a 3-D resistivity forward modelling program gave similar results where the direct method was much faster for models with a large number of electrodes. Our interest is in large 3-D resistivity surveys where the number of electrodes can exceed one million (Unrau, 2019). Most 3-D ERT surveys are carried out by small to medium sized geophysical service companies where the available computational tool is usually a consumer level PC or workstation. Thus, our research is geared towards computational solutions that can be implemented on PCs. We use the PARDISO (Schenk and Gartner, 2002) function in the Intel MKL library (Kalinkin and Kostin, 2013) for the numerical calculations. We note that several other publicly available direct solvers can also be used (Demmel *et al.*, 1999; Davis, 2006). The PARDISO function was used as it requires minimal additional computer code and the MKL library is optimised for Intel CPUs used in widely available and relatively inexpensive PCs.

One common class of direct solver methods is based on the Cholesky decomposition method (George and Liu, 1981). Here we briefly list the main steps involved and the reason for the speed advantage for problems with many sources. As shown earlier, the capacitance matrix equation is given by

$$\mathbf{C\Phi} = \mathbf{s}. \tag{2}$$

The first step is to factorise $\mathbf{C}$ into a triangular matrix ($\mathbf{L}$) product (George and Liu, 1981) as follows.

$$\mathbf{C} = \mathbf{LL}^{\mathbf{T}} \tag{3}$$

Many sophisticated algorithms have been devised to renumber the nodes in the mesh to reduce the number of non-zero elements in the $\mathbf{L}$ matrix (George and Liu, 1981; Demmel *et al.*, 1999; Schenk and Gartner, 2002; Davis, 2006; Devine *et al.*, 2006). This factorization step only has to be done once as the $\mathbf{C}$ matrix (and the $\mathbf{L}$ matrix) only depends on the mesh structure and the conductivity values of the mesh elements, and does not depend on the source vector $\mathbf{s}$. This is

followed by the solution step to calculate the potentials due to a current vector **s** which involves solving two matrix-vector equations. The first operation is to calculate a temporary vector **y** by solving

$$\mathbf{L}\mathbf{y} = \mathbf{s}. \tag{4}$$

The second operation is a back-substitution step that solves the following equation to determine the potential vector **Φ**.

$$\mathbf{L}^{\mathbf{T}}\mathbf{\Phi} = \mathbf{y} \tag{5}$$

As **L** is a sparse triangular matrix, the solution step is generally a fast operation which is repeated for each source position. If there is a large number of sources, the time taken by the factorisation step becomes much smaller compared to the total time taken by the solution steps. As an example, for the Bonsall Leys field data set used in this paper, the time taken by the factorisation step less than 2% of the total time taken to calculate the potentials. In comparison, for iterative methods, the full capacitance matrix equation (2) has to be solved repeatedly for each source position. Direct methods work well for the first order finite elements used in resistivity modelling where there are efficient techniques to renumber the nodes to reduce the number of non-zero values in the **L** matrix. The main limitation of direct methods is that the number of non-zeros in the **L** matrix is much greater than in the original **C** matrix. However, for resistivity problems, direct methods can process meshes with up to about 10 million nodes on a PC with 128GB RAM.

Results

In this section, we compare the inverse models obtained from the structured rectangular, semi-structured and adaptive semi-structured meshes for a synthetic model and a field survey data set. The inversions were carried out on a PC with a 16 core Intel 12900K CPU.

Synthetic model test

Figure 4 shows the synthetic model with six rectangular blocks embedded in a homogeneous medium of 50 Ωm. We arranged the electrodes in a 33 by 15 m rectangular grid with a 1 m spacing in both the *x* and *y* directions for a total of 495 electrodes. The test data set consisted of all the possible inline dipole-dipole array measurements in the *x* direction with a maximum geometric factor 4147 m (corresponding to a dipole array with '*a*' equals to 1 m and '*n*' factor of 10). This gave a total of 7860 data points. Gaussian random noise with an amplitude of 0.5 milli-Ω was added to the calculated resistance values (with a range of 2.6 to 13108.4 milli-Ω) before they were converted to apparent resistivity values (Zhou and Dahlin, 2003). This resulted in an average noise level of about 1.5% in the apparent resistivity values. The main purpose of this test was to compare the inverse models obtained using a normal dense rectangular mesh and the sparse semi-structured meshes. The model grid was extended by 3 m in both the *x* and *y* directions beyond the central area covered by the electrodes. The inverse model had nine layers giving a total of 6840 cells. We use the L1-norm constraint (Farquharson and Oldenburg, 1998) for the model roughness and data misfit in the inversion algorithm.
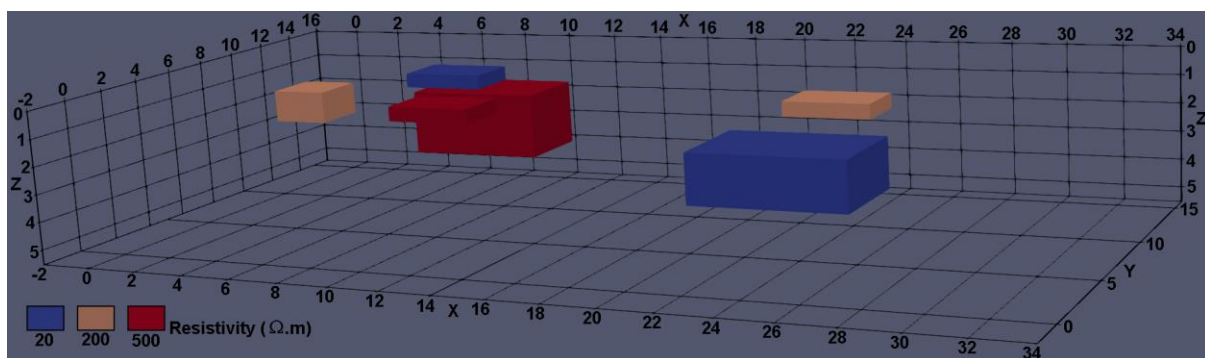

Figure 4 Synthetic test model with six rectangular blocks embedded in a homogeneous medium (transparent in the plot) of 50 Ωm.

Figure 5a shows the inverse model obtained using a structured rectangular finite-element mesh with 418100 nodes. To determine the accuracy of the inverse models, the following equation was used to calculate the relative difference (∂) between the resistivity of the true (r_t) and inverse (r_i) models:

$$\partial(j) = 100 \times [r_i(j) - r_t(j)]/r_t(j) \tag{6}$$

where j is the cell number. We calculated the average percentage relative difference (∂_a) using the following equation,

$$\partial_a = [\Sigma_1^m |\partial(j)|]/m \tag{7}$$

where m is the number of model cells. For the inverse model obtained using a dense rectangular mesh, the average difference is 3.73% (Table 1).

Figure 5b shows the inverse model obtained using a semi-structured mesh. The top five mesh levels used four mesh lines per model cell while the sixth and seventh mesh levels used two mesh lines, follow by one mesh line for the deeper mesh levels. The model misfit was marginally higher at 3.81% (Table 1). Tests were conducted using three to six dense mesh levels. All the inverse models had data misfit of 1.5% (with differences of less than 0.05%). Between six and four dense mesh levels, there was a small increase in the model misfit. However, the difference in the model misfit compared to the rectangular mesh model is only 0.20% with four dense mesh levels. The difference in the model misfit was much lower than the data noise level of 1.5%. When we used three dense mesh levels, the model misfit increased to 3.99%. When the depth to the deepest dense mesh level is more than the smallest spacing between two electrodes in an array (1 m in this synthetic test model), the increase in the model misfit compared to a structured rectangular mesh was not significant. The gradient of the potential near an electrode is high, and the rate of change in the gradient decreases with increasing distance from the electrodes. At depths below one unit electrode spacing, a sparser mesh had a smaller effect on the calculated potentials.

The model misfit obtained using the adaptive semi-structured mesh (3.95%) with 5 dense mesh levels is about the same as the semi-structured mesh model (with differences of less than 0.05%). A buffer zone of one model cell (with two nodes) was used between the dense cells (with four) nodes and the outer sparse cells (with one node). Increasing the buffer zone to two cells did not significantly change the results.

Table 1 also shows the number of nodes in the mesh and inversion calculation time with the different meshes. The semi-structured meshes have about one-third the number of nodes of the structured rectangular mesh. The calculation time is slightly more than one-third. The adaptive semi-structured mesh further reduced the number of nodes and calculation time by about 11% compared with the semi-structured mesh with the same number of dense upper levels. In this simple example, the sparser cells are confined to the two outermost rows and columns next to the edge of the model grid, so the reduction in the number of nodes and calculation time by the adaptive method is not very large.

The average data and model misfits are convenient measures of the accuracy of the models as they reduce the differences to a single number. However, they do not give information about the spatial distribution of the misfits. We next show the misfits in the form of 3-D scatter plots and histograms. Figure 6a shows the 3-D scatter plots for the apparent resistivity values calculated for the synthetic model that was used as the input data for the different inversion tests. The (x, y) position of each data point is given by the centre of the array, while the z position is given by the median depth of investigation of the array (Edwards, 1977; Barker, 1989). There are some higher or lower values in the vicinity of the anomalous blocks in the model. The scatter plot for calculated apparent resistivity values from the rectangular mesh model is shown in Figure 6b for comparison. It is difficult to detect any significant differences between the two plots. Figures 6c and 6d show the data misfit plots for the rectangular and adaptive semi-structured mesh models. The overhead oblique views show some higher misfits (positive and

negative) in the vicinity of the anomalous blocks. The side views show higher data misfits at a few data levels corresponding to arrays with higher geometric factors. The geometric factor for the dipole-dipole array (G_d) is given by

$$G_d = \pi a(n+1)(n+2)(n+3), \tag{8}$$

where 'a' is the dipole length, and 'n' is the ratio of the distance between the current and potential dipoles to the dipole length. The geometric factor is proportional to n^3, so arrays with the higher n factors would be expected to be noisier. Histogram plots for the data misfits for the rectangular and adaptive mesh models are shown in Figure 7. They are fairly similar with the mode in the -0.5 to +0.5 percent range. The histogram plots of the model misfits for the rectangular mesh and adaptive mesh models are fairly similar (Figure 8). There are slight differences in the bars for the 1 to 2 and 2 to 3 percent ranges, probably due small changes in members that lie close to the 2 percent misfit value.

In this synthetic example, the model mesh is much smaller than the field data sets for which this method is generally intended, and we expect larger gains in the calculation time using the semi-structured mesh techniques for problems involving more than 1 million nodes.
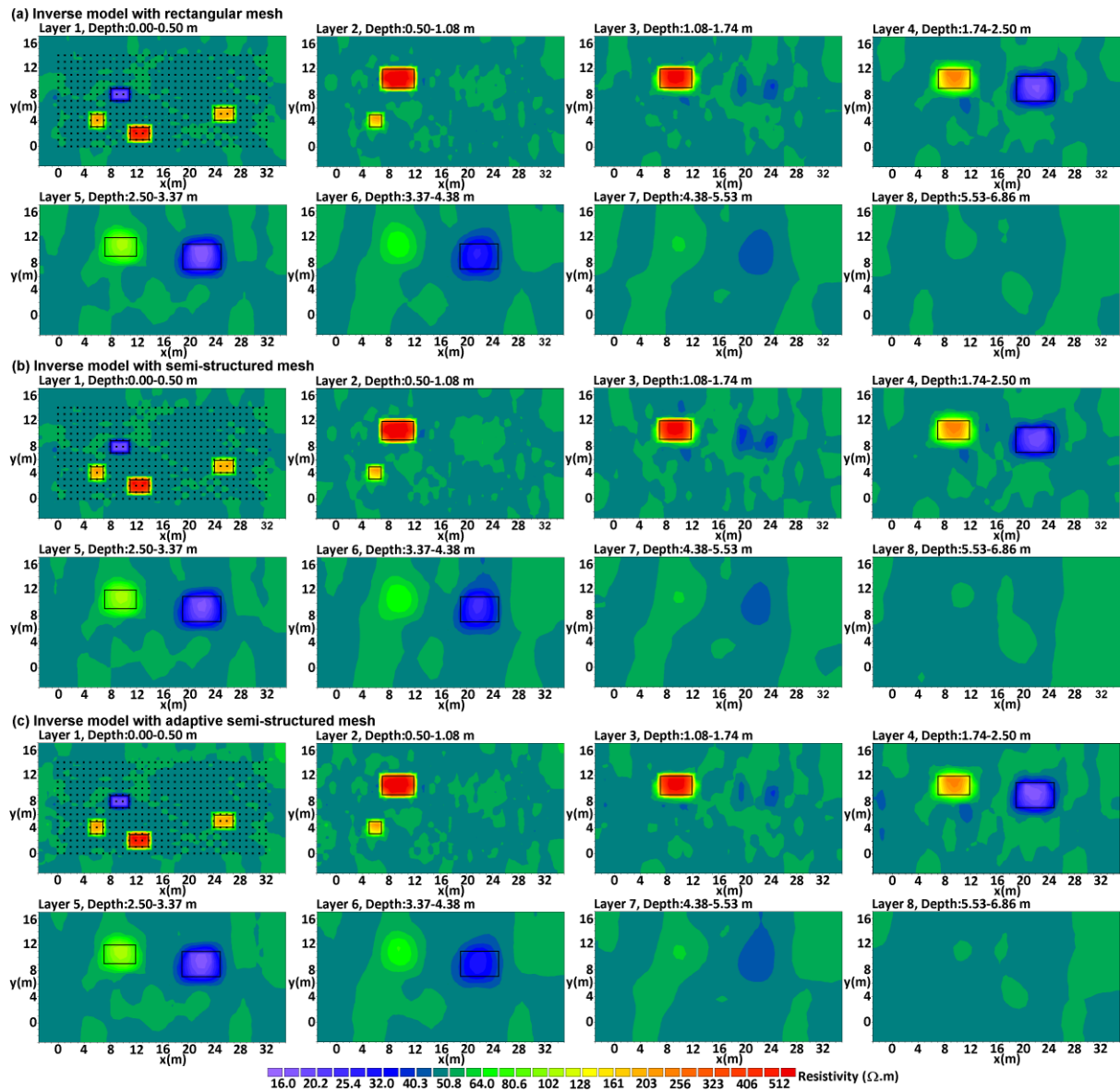
Figure 5 Inverse models (plan view) obtained with a (a) rectangular mesh and (b) semi-structured mesh with top five dense mesh levels (c) adaptive semi-structured mesh. The actual positions of the rectangular blocks are marked by black outlines. The data misfit for all inverse models is 1.5%. The electrodes are marked by small black squares in the top layer in (a), (b) and (c).

Table 1 Inverse model properties for synthetic data set with different types of meshes. All the inverse models took 8 iterations to converge and have a data misfit of about 1.5%.

Type of mesh	Number of dense mesh levels (depth)	Number of nodes	Model Misfit (%)	Calculation time (s)
Structured	20 (46.57)	418100	3.73	111
Semi-structured	6 (2.50)	152414	3.81	49
Semi-structured	5 (1.74)	140724	3.85	45
Semi-structured	4 (1.08)	129034	3.93	44
Semi-structured	3 (0.50)	117344	3.99	39
Adaptive	5	123644	3.95	40

Figure 6. Oblique and side views of scatter plots for synthetic test model showing (a) measured and (b) calculated (rectangular mesh model) apparent resistivity values. Plots of apparent resistivity data misfits for (c) rectangular mesh and (d) adaptive semi-structured mesh inverse models.
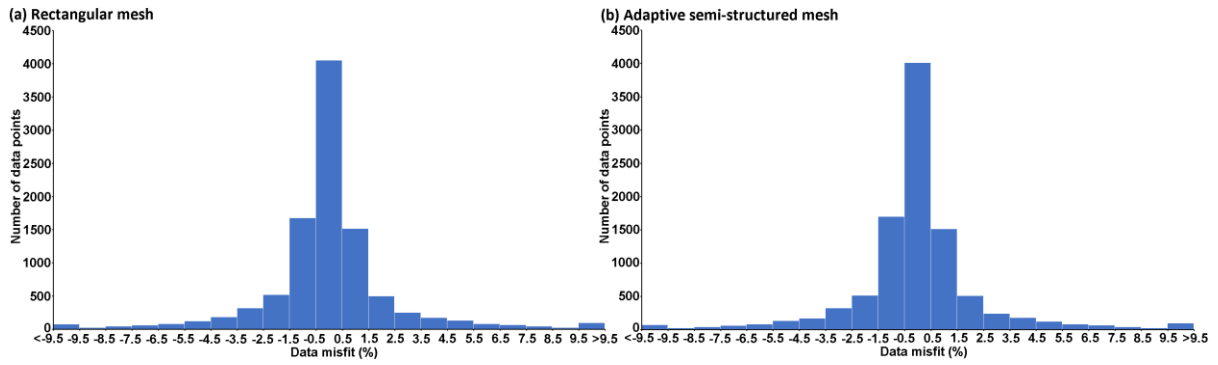
Figure 7. Histogram plots of the data misfits for the (a) rectangular mesh and (b) adaptive
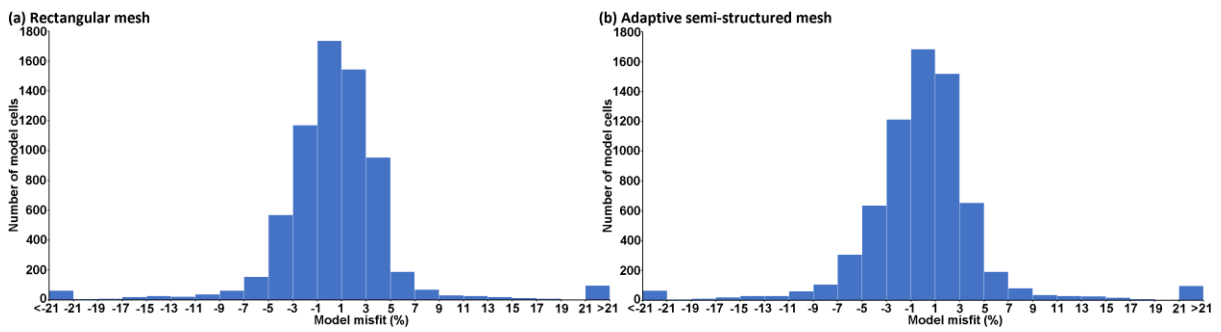
mesh inverse models.

Figure 8. Histogram plots of the model misfits for the (a) rectangular mesh and (b) adaptive

mesh inverse models.

Field survey example

Mobile surveying systems can generate data sets with over a million unique electrode positions and data points (Unrau, 2019; Loke *et al.*, 2020). The inverse model might have a similar number of model cells. Small geophysical organisations commonly use PCs or workstations to model data acquired from a survey. To carry out an inversion of such large data sets poses significant challenges with limited computer resources. Therefore, any gain in processing speed can increase the utility of 3-D electrical resistivity for many.

We used a field data set that was acquired in order to detect historic mineshafts in the Bonsall Leys area in Derbyshire, U.K. (Kuras *et al.*, 2003). The area is underlain by limestone with interbedded basalt at a depth of about 20 m. Lead had been mined with many vertical shafts from extensive extraction operations in the 19th century. Mineralisation of the limestone takes the form of extensive vertical sheets perpendicular to the bedding that contain a variety of minerals, including lead sulphide (galena).

A towed capacitively coupled system, the BGS CRI (Capacitive Resistivity Imaging) system (Kuras *et al.*, 2007), was used to dynamically acquire the apparent resistivity data with five channels in an equatorial dipole-dipole configuration (Figure 9a). The dipole length was 1.5 m with dipole separations ranging from 1.6 m to 5.4 m. Flat plates were used as the electrodes in this system. Towing speeds equaled a slow walking pace of ~1.5 km/hr, and a practically continuous path was followed to cover the survey area of interest. A discussion on the advantages and disadvantages of different types of capacitively coupled systems can be found in Kuras (2002) and Kuras *et al.* (2006).

The data set had 898,076 electrode positions and 381,219 data points. The roughness filter matrix (**W** in equation (1)) also had components in the diagonal directions to reduce 'banding' effects in the *x* and *y* directions of the model grid (Loke and Dahlin, 2010). We also used the wavelet compression method to reduce the computer memory required by the Jacobian matrix

and the time to solve the least-squares equation (Davies and Li, 2013; Loke *et al.*, 2020). Loke *et al.* (2021) used a subset of the data set with 418,331 electrode positions and 207,997 data points from the central part of the survey area with more uniform data coverage to test the semi-structured mesh method. In this paper, we used the entire data set that has significant areas without data coverage at the corners and sides of the model grid (Figure 10). The inverse model had 10 layers and 127,680 cells that resulted in a Jacobian matrix with 48,674,041,920 values. The wavelet compression method (after removing components with amplitudes of less than 1% the maximum amplitude) reduced the size of the Jacobian matrix to 379,837,000 values, or about 0.8% of the full Jacobian matrix.

The survey data set has nearly nine hundred thousand unique electrodes positions. A modification was made to the algorithm used to calculate the potential values in order to reduce the calculation time. The calculation of the Jacobian matrix using the adjoint equation method uses the potential at all the nodes of the mesh due to current sources at the locations of both the current and potential electrodes (McGillivray and Oldenburg, 1990; Loke *et al.*, 2020). This is normally done by solving the capacitance matrix equation (2) for each electrode position (where the **s** vector on the left-hand side has a single non-zero value), one by one. The four sets of potential values for the two current and two potential electrodes used by the array (such as A, B, M_1 and N_1 in Figure 9b) are then combined to calculate the apparent resistivity and Jacobian matrix values. This is usually the most efficient method for data sets measured using multi-electrode systems where each electrode along the cable can be used as a current or potential electrode, such as for the synthetic data set. In the resistivity meter systems used for mobile surveys, the relative positions of the current and potential electrodes are fixed and only a limited number of array configurations can be measured. In particular, the system used for the Bonsall Leys survey has a fixed equatorial dipole-dipole configuration with five arrays consisting of the current dipole AB and the five MN potential dipoles (Figure 9b). As the

system is moved continuously during the survey, the positions of the electrodes from a subsequent set of measurements usually do not coincide with those from a previous measurement. Twelve different solutions of the capacitance matrix equation are then needed to determine the potentials due to all the electrodes (A, B, M_1, N_1, M_2, N_2, M_3, N_3, M_4, N_4, M_5, N_5). Instead of calculating the potentials due to twelve individual electrodes, the same information can be obtained by calculating the potentials due to six dipoles (AB, M_1N_1, M_2N_2, M_3N_3, M_4N_4, M_5N_5). The current vector **s** now has two non-zero values corresponding to the two electrodes in the dipole. This reduces the time by the solution steps in equations (4) and (5) of the direct method used to calculate the potentials by half. The required potentials calculated using individual electrodes or dipoles are mathematically the same. Another common configuration used by mobile surveying systems is the inline dipole-dipole array (Inazaki, 2007; Unrau, 2019; Loke *et al.*, 2020). The inline dipole-dipole arrangement shown in Figure 9b has eight individual electrodes and six dipoles. The calculation time would be reduced by 25% if the calculations are made using dipoles instead of individual electrodes. The reduction in calculation time is less but still would be worthwhile for very large surveys with more than a million electrode positions (Unrau, 2019).
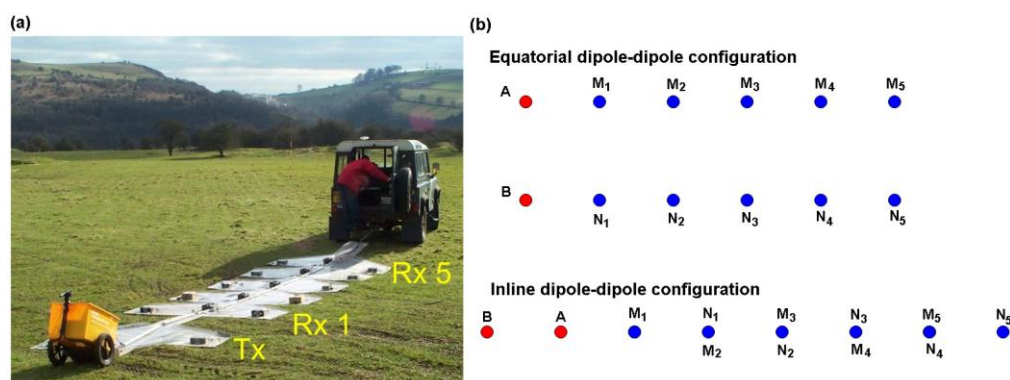

Figure 9 (a) Bonsall Leys field survey with mobile array. (b) Arrangement of electrodes in mobile systems using the equatorial and inline dipole-dipole arrays.
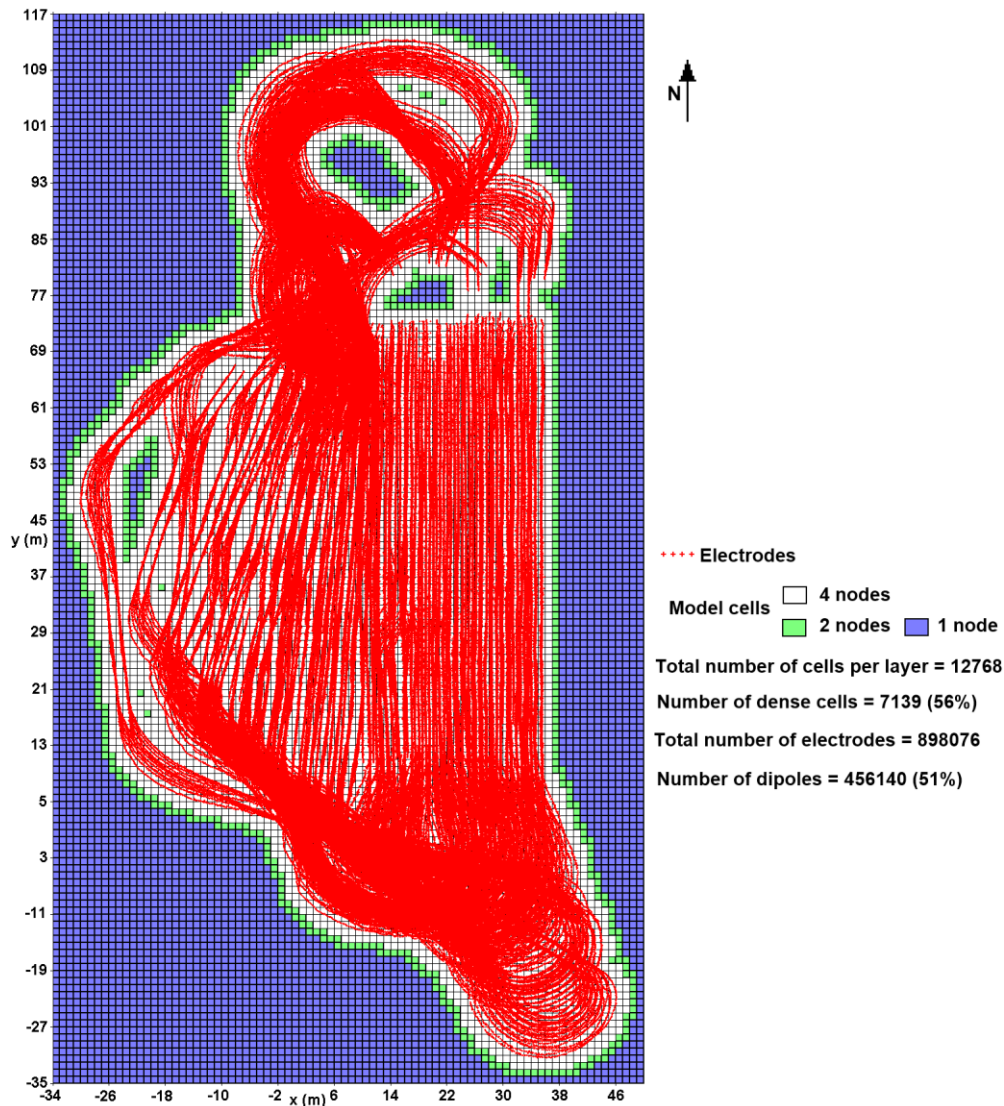
Figure 10 Bonsall Leys field survey tracks with model grid.

The inverse model for the Bonsall Leys survey data set, using a dense rectangular structured mesh (with 5,203,638 nodes), is shown in Figure 11a. Equation (1) contains a damping factor term λ that gives the relative weight for minimising the model roughness compared to the data misfit. As λ is reduced, the data misfit decreases at the expense of increasing the model roughness. If λ is too large, an overly smooth resistivity model with a high data misfit will be obtained. If λ is too small, the model can show large unrealistic resistivity variations as the algorithm attempts to fit the noise to lower the data misfit. Ideally there is an optimum value of λ that gives a model with a satisfactory data misfit with minimal artefacts. For the synthetic data set the average noise level is known, so the model that has a

data misfit close to the noise level can be selected. However, for this field data set, the noise level is not known (no reciprocal or repeat measurements were made due to the operational constraints of the towed-array CRI method). Therefore, the optimum damping factor and associated data misfit has to be estimated from the inversion process itself. We use an inversion algorithm with a slow cooling sequence (Oldenburg and Li, 2005; Haber *et al.*, 2007) that starts with a large value for λ which is reduced by a small amount after each iteration. This produces a series of inverse models with different data misfits and model roughness. We use the following equations to calculate the L1-norm average data misfit (*D*) and model roughness (*M*) for each iteration:

$$D = \frac{1}{d} \sum_{i=1}^{d} |g_i| \qquad (9)$$

$$M = \frac{1}{m} |\mathbf{Wr}| \qquad (10)$$

where *d* is the number of data points while *m* is the number of model parameters. The L-curve method (Farquharson and Oldenburg, 2004) is then used as a post-inversion tool (Loke *et al.*, 2022a; Loke *et al.*, 2022b) to determine the optimum damping factor. Figure 12a shows the L-curve plot of the model roughness versus the data misfit for the Bonsall Leys inverse models. Figure 12b shows a plot of the curvature of the L-curve. We select the optimum damping factor at the maximum point of the curvature plot (Farquharson and Oldenburg, 2004), which has an associated data misfit of 7.3%.

The computational time for the structured mesh model took 294,591 seconds (81.8 hours) and 8 iterations for the inversion program to converge. A known mine shaft appears as a high resistivity anomaly in the second and third model layers (Figure 11a). There is a prominent narrow low resistivity linear anomaly in layers 3 to 6 which could be due to a mineralised sheet with conductive minerals, such as galena, previously mined in this area. There is also an interesting diffused low resistivity linear anomaly below the mine shaft which

could be a mined out mineralised sheet. This anomaly was less clear in a previous inversion using subset of the data set (Loke *et al.*, 2021).

For the semi-structured mesh model, we used five dense mesh levels, which resulted in a mesh with 1,555,313 nodes (about 30% of the structured rectangular mesh). The inversion took 84120 seconds (23.4 hours) or about 25% of the time taken by the structured rectangular mesh (Table 2). There were no visible differences between the models obtained with the rectangular structured and semi-structured meshes (Figure 11b). Since the true resistivity of the subsurface was not known, we calculated the relative difference between the rectangular structured and semi-structured mesh models using equations (6) and (7). There was an average difference of 0.58% in the resistivity values which was not significant compared to the data misfit of 7.3%.

Figure 13a shows the inverse model obtained with the adaptive semi-structured mesh. The number of nodes was reduced by about 80% compared to the rectangular mesh (Table 2). The inversion time taken was 63204 seconds (17.6 hours), or about 21% of the time taken by the structured rectangular mesh. The average difference in the inverse model resistivity values was 0.61% which is almost the same as the semi-structured mesh model.
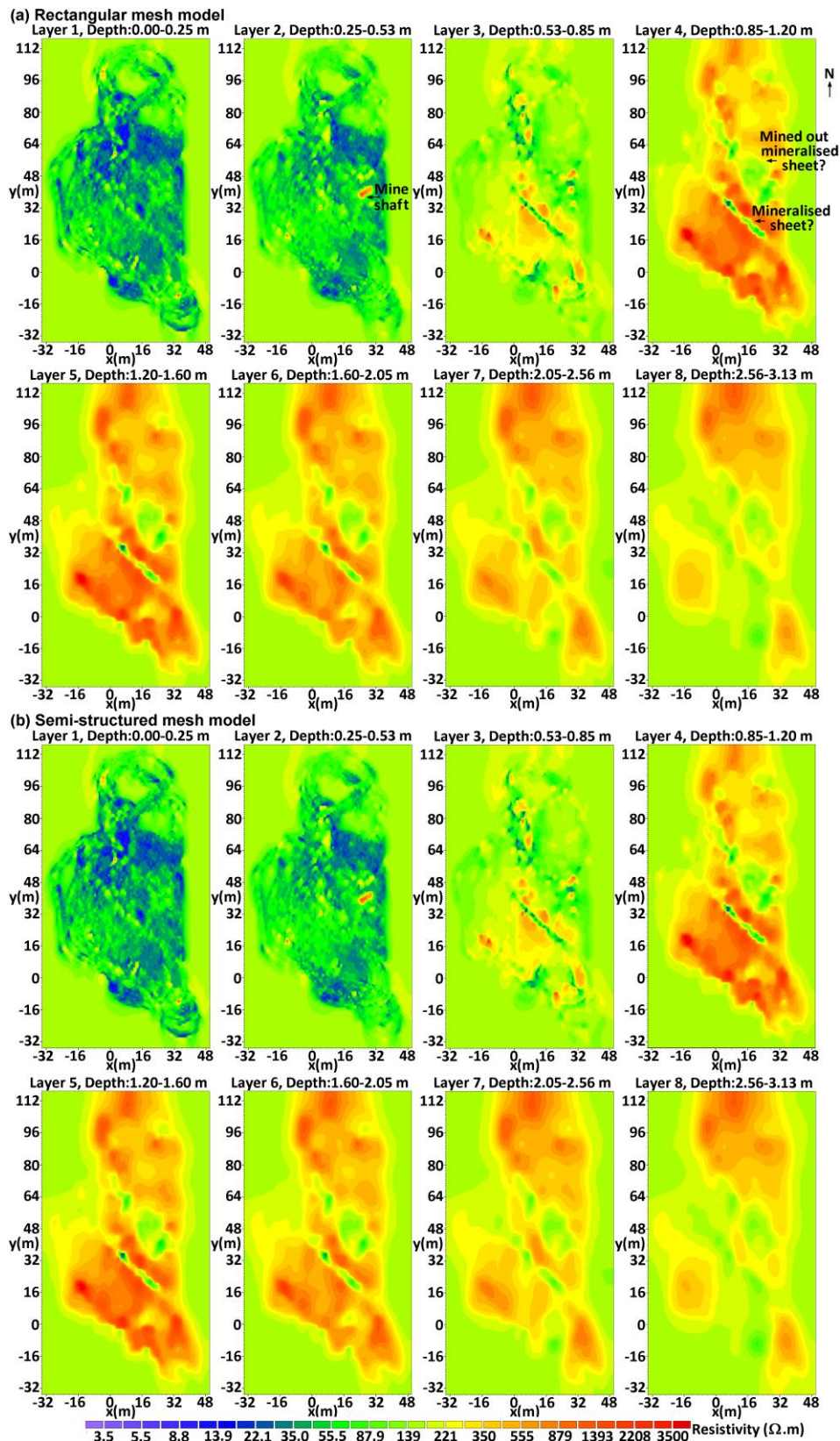
Figure 11 Bonsall Leys inverse models (plan view) using (a) a dense rectangular mesh, and (b) semi-structured mesh with five dense mesh levels. The position of the mine shaft is marked in the second layer of (a). The data misfit for both models is 7.3%.

As a final test, we combined the adaptive semi-structured mesh technique with the segmentation method (Loke *et al.*, 2020; Yang *et al.*, 2014; Cox *et al.*, 2010; Loke and Lane, 2004; Christiansen and Auken, 2004) where the mesh was subdivided into eight overlapping segments. The average number of nodes in each sub-mesh was 253,490 and the calculation time was 18,029 seconds (5.0 hours), which was about 6% of that taken by the structured rectangular mesh (Table 2). The average difference in the inverse model resistivity values compared to the rectangular mesh model was marginally higher at 0.71%. This was also much smaller than the data misfit. The inverse model shown in Figure 13b was almost identical to the rectangular structured mesh model (Figure 11a). There were very small differences in the 8th layer which was not surprising due to the reduction in resolution with depth. The differences were very minor and conceptually would not alter a geological interpretation of the results.

Figures 14a and 14b show the apparent resistivity scatter plots for the measured and calculated (for the rectangular mesh model) apparent resistivity values. Both plots look very similar making it difficult to identify differences between them. Figure 14c shows the scatter plot for the data misfits which helps to identify areas where the measured and calculated values differ significantly. There are clusters of data points with higher data misfits (blue and red points) near the southern and northern ends of the survey tracks (Figure 14c, left side). These might be caused by errors in the positions of the electrodes where the survey lines turn. The actual positions of some of the electrodes might differ from the assumed positions recorded due to bending of the survey lines. This phenomenon had been previously observed in surveys using the inline dipole-dipole array (Loke *et al.*, 2020; Unrau, 2019). Usually, the positions of the electrodes are estimated by using one or at most two GPS receivers. The data misfit obtained by Loke *et al.* (2021) that used the data points from the central part of the survey (where there was more uniform data coverage) had a lower data misfit of 6.6% compared to

7.3% for the entire data set. This is probably because the entire data set includes data points

from the southern and northern ends of the survey region that have noisier data points. A side

view plot of the data misfit (Figure 14c) shows an interesting pattern where the second and

fourth data levels have slightly higher misfits. This is probably caused by some instrumentation

issues for the two measuring channels at the M_2N_2 and M_4N_4 potential dipoles (Figure 9b).

This is only revealed in the data misfit scatter plot (Figure 14c) and not clear in the apparent

resistivity plot (Figure 14b). The data misfit scatter plot for the adaptive semi-structured mesh

model (Figure 14d) is very similar to the rectangular mesh model (Figure 14c) with no obvious

differences. The histogram plots for the two set of data misfits are also very similar (Figure 15)

with the mode in the -2% to +2% range. Figure 16 shows histogram plots of the difference in

the inverse model resistivity values from the different sparse meshes from the rectangular mesh

model. They are fairly similar with most of the misfit values in the -0.5% to +0.5% range.

There is a small difference in the plot for the inverse model with segmentation (Figure 16c)

which is probably due to differences in the deeper layers that have poorer resolution.
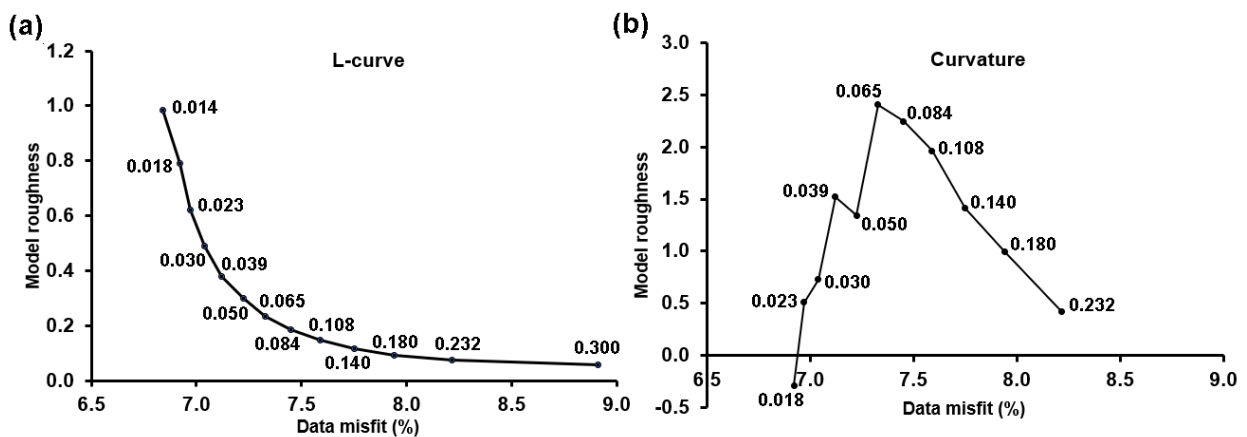

Figure 12 Bonsall Leys field data set (a) L-curve plot and (b) L-curve curvature plot. We list

the damping factor next to the points on the curves.

Table 2 Inverse model properties for Bonsall Leys field data set with different types of meshes. The average number of nodes in a segment is listed for the adaptive mesh with 8 segments. All the inverse models have a data misfit of about 7.3%.

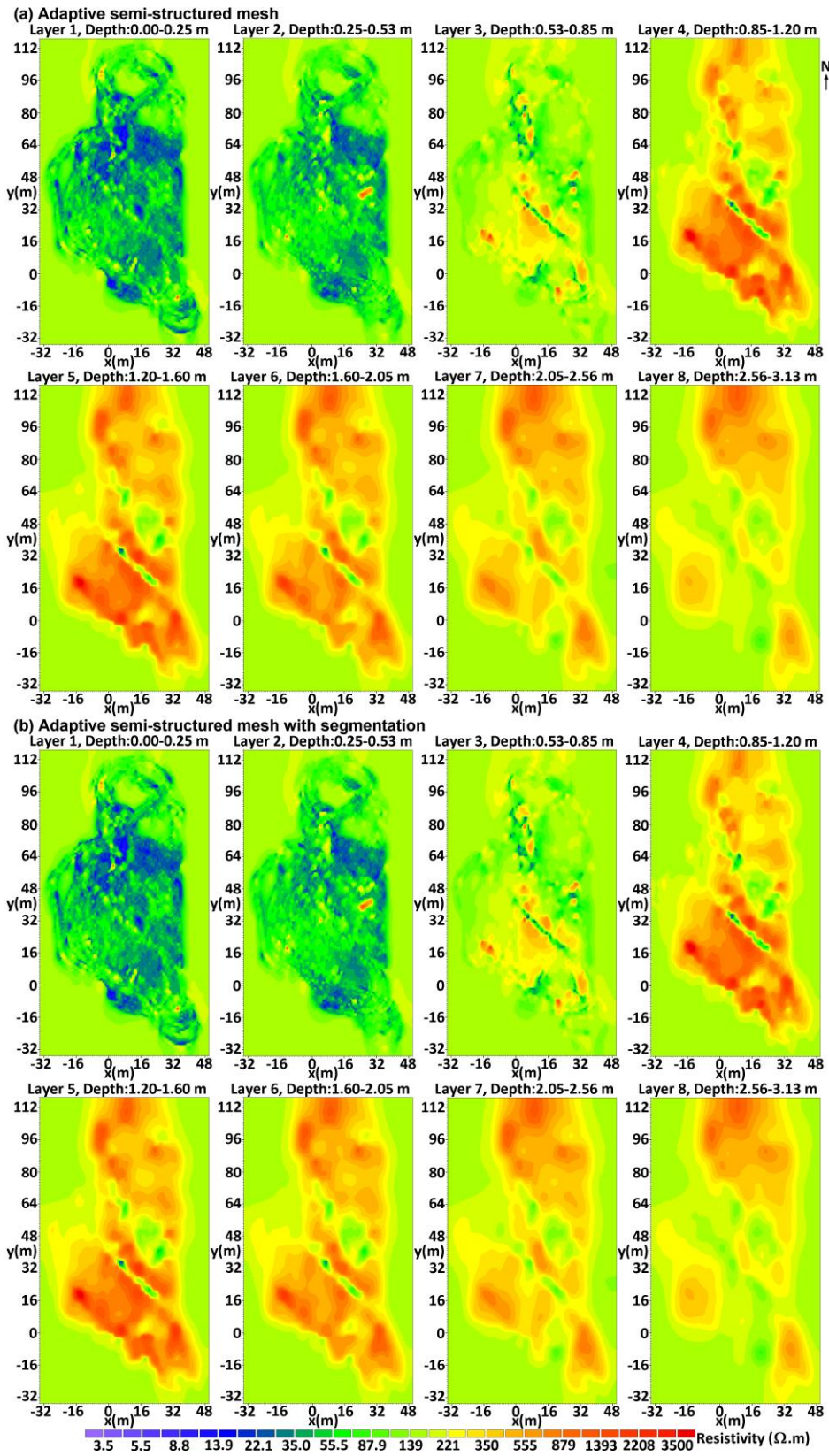| Type of mesh	Number of dense mesh levels	Number of nodes	Model Difference (%)	Calculation time (s)
Structured	22	5,203,638		294,591
Semi-structured	5	1,555,310	0.58	87,721
Adaptive	5	1,091,880	0.61	63,204
Adaptive with 8 segments	5	253,490	0.71	18,933

Figure 13 Bonsall Leys inverse models using (a) adaptive semi-structured mesh and (b) adaptive mesh with segmentation method. The data misfits for both models are 7.3%.
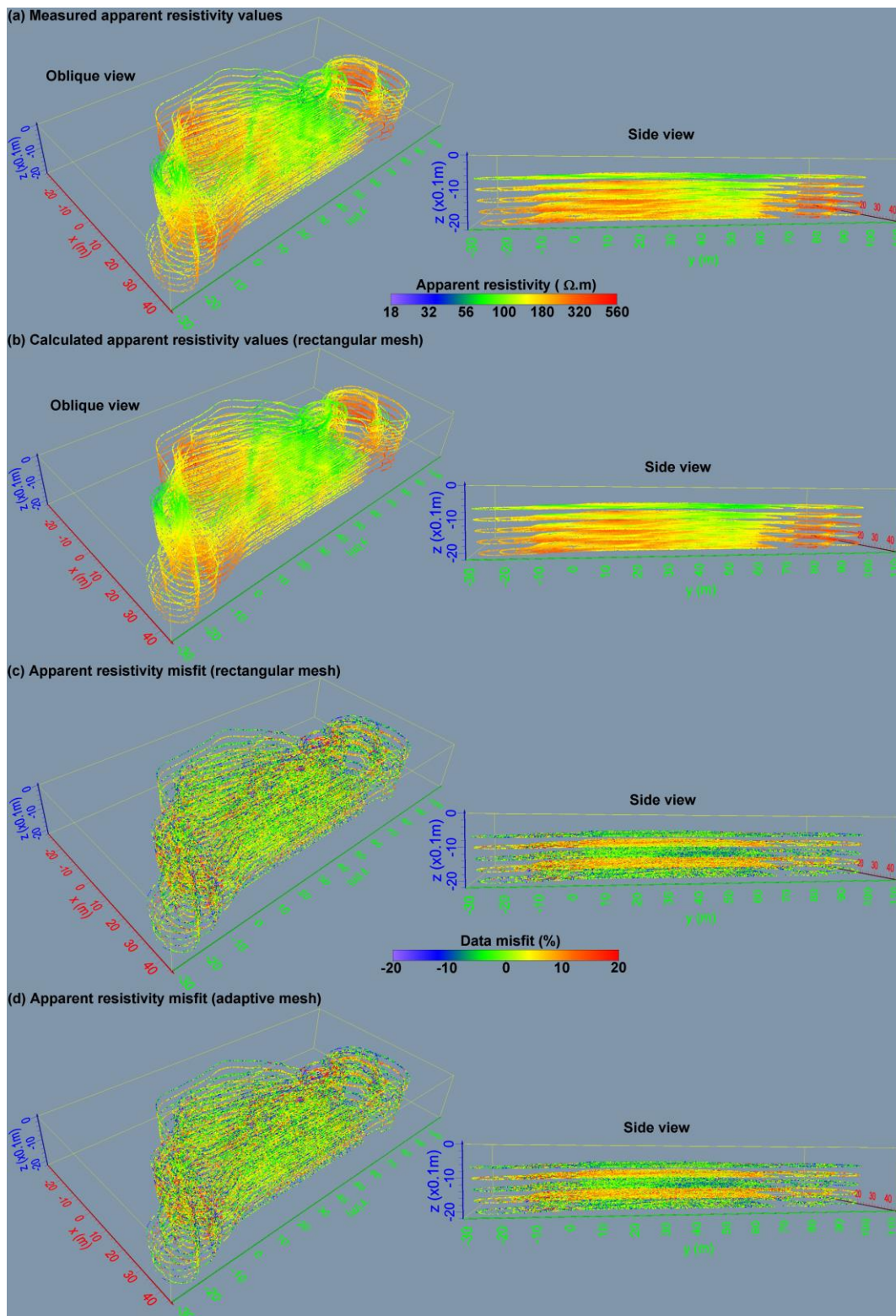
Figure 14 Oblique and side views of scatter plots for the Bonsall Leys data set showing (a) measured and (b) calculated (rectangular mesh model) apparent resistivity values. Plots of apparent resistivity data misfits for (c) rectangular mesh and (d) adaptive semi-structured mesh inverse models. Note the vertical axis has a vertical exaggeration of 10.
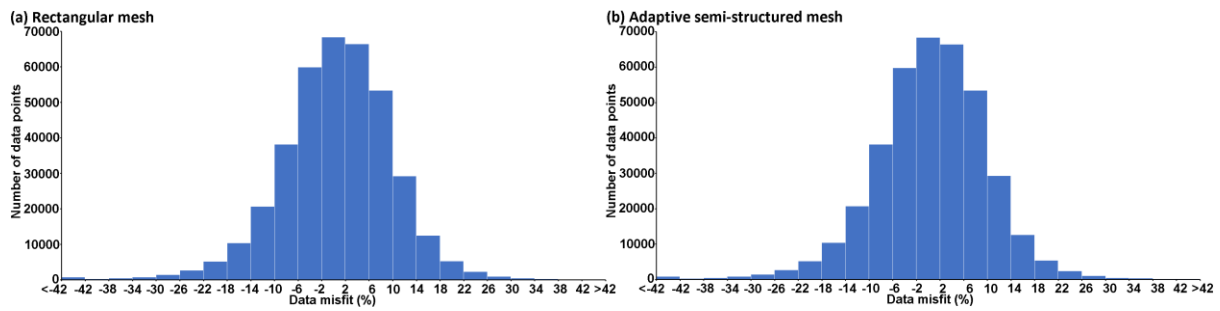
Figure 15. Bonsall Leys survey histogram plots of the data misfits for the (a) rectangular mesh and (b) adaptive semi-structured mesh inverse models.
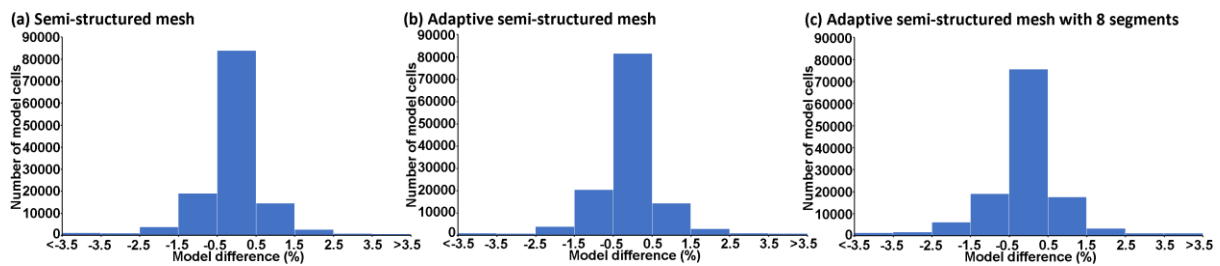

Figure 16. Bonsall Leys survey histogram plots of the difference in the model resistivity values with rectangular mesh model for (b) semi-structured, (b) adaptive semi-structured and (c) adaptive semi-structured (with 8 segments) mesh inverse models.

Discussion

Using a model grid with the cells arranged in a structured rectangular pattern has several advantages. It is easier to modify the distribution of the cells and roughness filters to emphasize structures in selected directions to more closely fit with the known geology. It is also easier to optimise the wavelet compression method to reduce the memory required by the Jacobian matrix by converting it to a 1-D function which also reduces the time to solve the least-squares equation with the linear conjugate gradient method (Loke *et al.*, 2020). The normal rectangular finite-element mesh for such a model grid has the disadvantage of an unnecessarily fine mesh

in regions far from the electrodes which results in a large number of nodes. This increases the computer memory and calculation time to solve the finite-element capacitance matrix equation and to calculate the Jacobian matrix. We adapt some of the techniques of the unstructured mesh method in order to reduce the number of nodes by using a dense mesh near the surface where the electrodes are located and a sparser mesh in regions further from the electrodes in the semi-structured mesh (Loke *et al*., 2021) technique. Hexahedral elements are used in most of the mesh, while tetrahedral elements are used to connect regions with different node densities. This reduces the number of nodes by about three times and the calculation time by more than three times for the Bonsall Leys field data set. A new adaptive semi-structured mesh technique is presented that also reduces the number of nodes in the model cells at the upper levels that are further than one unit electrode spacing from the nearest electrode. It reduces the inversion time for the field data set by more than four times without significant changes to the inverse model.

When the adaptive semi-structured mesh technique is combined with the segmentation method, we reduced the calculation time by about fifteen times. The average difference in the inverse model resistivity values with the structured rectangular mesh model is less than one percent which is not significant for field data sets where the data noise level is frequently higher (particularly for mobile surveys).

Günther and Rücker (2018) described a mixed mesh setup with a structured mesh for the inner rectangular model grid region, and an unstructured mesh between the inner region and the boundaries of finite-element mesh. This arrangement uses a dense rectangular mesh in the model grid zone for all the mesh levels up to the depth of the deepest model layer. The semi-structured mesh described in this paper uses fewer nodes by progressively reducing the node density with depth below the first four or five mesh levels within the model grid zone.

We note that similar methods using rectangular mesh elements to reduce the number of nodes had been devised using the OctTree (Haber and Heldmann, 2007) and multi-resolution

(Cherevatova *et al*., 2018) techniques for EM modelling. The paper by Gao *et al.* (2020) who adapted the multi-resolution grid technique to resistivity modelling is probably more directly relevant to the present work. All these methods are based on the finite-difference method using rectangular mesh cells. Two reasons were cited by Haber and Heldmann (2007) for choosing the finite-difference method, which are the longer times take by the meshing tool to construct the unstructured grid and to assemble the elements of the capacitance matrix for the finite-element method. For the large 3-D field example in this paper the total time taken to construct the adaptive semi-structured grid and assemble the capacitance matrix was less 1% of the total calculation time, so they are not important factors in choosing the finite-difference over the finite-element method for large 3-D ERT problems. One disadvantage of using the finite-difference method in ERT modelling is that many surveys are carried out in areas with significant topography. Gao *et al*. (2020) describes a method to model the topography by using a number of very fine vertical mesh levels that approximates a slope by a series of small rectangular steps. As an extreme example, the survey area described by Udphuay *et al*. (2011) has a topography range of at least 260 m mapped by survey lines using an electrode spacing of 2 m. If the topography is modelled by rectangular steps of 1 m, more than 200 additional vertical mesh levels would be needed which would result in a very large 3-D mesh. This makes it impractical to use the finite-difference method for ERT surveys in areas with significant topography. In comparison, the finite-element method can easily model the topography by using a deformed mesh that drapes over the measured topography (Loke, 2000) without the need for additional mesh levels or nodes. The method described in Gao *et al*. (2020) seems to be tied to the iterative multigrid plus preconditioned conjugate gradient methods to solve the capacitance matrix equation. As discussed in an earlier section, it was demonstrated by Oldenburg *et al*. (2013) that direct methods to solve the EM capacitance matrix equation are up to several hundred times faster than iterative methods for problems with a large number

(100 to 1000) of sources. The methods described in this paper have been used for ERT surveys with more than a million sources where the speed advantage of the direct method is probably greater.

One possible improvement to the adaptive semi-structured technique is a different method to assign the node density for a mesh cell based on the model resolution (Day-Lewis *et al*., 2005). At present, a heuristic rule is used based on the distance of a mesh cell from the nearest electrode which does not take into account other factors such as the local data density. A possible improvement is to use the model resolution which is also affected by the data density near the mesh cell. The Jacobian matrix for a homogenous half-space (which can be calculated analytically) can be used as an approximation to calculate the resolution values for the data and model configurations used.

The adaptive semi-structured technique still retains the rectangular arrangement of the model cells (for example as in Figure 10). With a rectangular arrangement, it is relatively simple to convert the 3-D Jacobian matrix into a continuous 1-D function using a zigzag cell numbering scheme (Loke *et al*., 2020). The 1-D Jacobian function can then be reduced to a small number of components with significant amplitudes using a 1-D wavelet transform. A possible refinement is to retain only the first model cell with 1 node (purple colour in Figure 10) that borders the denser inner cell with 2 nodes (green colour in Figure 10) near the edges of the grid. This would involve a shift of at most only one cell in the x direction at the ends of each y row. A study needs to be made of the effect of the new scheme on the efficiency of the wavelet transform to compress the Jacobian versus the benefit from the reduction in the number of model parameters.

~~Figure 10 shows that in some areas with dense data coverage the survey tracks cross each other so there is probably redundant data. Yang *et al*. (2014) used random removal of data points which is simple to implement but has the disadvantage of possibly removing data points~~

~~from regions with low data density. A better method might be to systematically remove data points that makes the least contribution to the model resolution by using array optimization techniques developed by Wilkinson *et al*. (2006) and Loke *et al*. (2015).~~ Yang *et al.* (2014) devised an adaptive method for 3-D EM inversion that uses a data subset with a small number of soundings chosen randomly for the initial iteration (which has a high damping factor) which is gradually increased with each iteration as the damping factor is slowly reduced. If at an iteration the data misfit is not sufficiently reduced, the number of soundings is increased. This corrects for any bias in the model in the earlier iterations caused by under-sampling at certain regions. We are studying an alternative method that uses array optimization techniques (Wilkinson *et al*., 2006; Loke *et al*., 2015) to select the data subset for each iteration. Mobile surveys frequently have highly non-uniform data coverage. Some areas have dense data coverage where the survey tracks cross each other and some areas have sparse data coverage (Figure 10). For each iteration, the proposed method selects the data subset (which is also increased with each iteration) that gives the maximum average model resolution.

An approach that targets the cause of the higher data misfits in the field data set is needed to get the maximum benefit from the research effort needed. The source of noise in different geophysical methods can be very different (for example EM versus ERT). For the mobile ERT surveys, the error in the assumed positions of the electrodes is probably one of the largest sources of noise. ERT surveys use four electrodes (two transmitters and two receivers) with appreciable finite distances between them for each measurement and the calculated apparent resistivity value depends on the assumed positions of the electrodes. Airborne EM surveys use the same loop as the transmitter/receiver, so an error in the position does not significantly affect the input data. One possible research problem is to devise an algorithm that estimates the errors in the positions of the electrodes that will minimise the data misfit. Previous research by Wilkinson *et al*. (2016) and Loke *et al*. (2018) on calculating the shifts in electrode

positions down a slope due to soil movements might be relevant, although the slope problem is simpler as the true initial positions of the electrodes are known. A possible algorithm is to first invert the data set by changing the model resistivity values only until the desired data misfit is reached (as determined by the L-curve method). After that, the model resistivity values are fixed and the least-squares optimisation method is used to find changes in the electrode positions that will further reduce the data misfit.

We are also studying the use of different polynomial approximations (such as linear, trilinear, quadratic) for the potential function within the hexahedral and tetrahedral elements used in finite-element method in an effort to improve the accuracy of the calculated potentials. The conformal mesh generated by the semi-structured methods ensures that the potential is continuous at the nodes shared by different elements. A study needs to be made on the continuity of different polynomial functions at the common faces shared by adjacent elements (such as a trilinear polynomial for hexahedral elements and linear polynomial for tetrahedral elements) and its effect on the calculated potentials at the nodes.

Research is also being carried out on computational techniques to further reduce the calculation time, such as carrying out the numerical calculations using GPUs (Rennich *et al.*, 2016; Yeralan, 2017; Zachariadis *et al.*, 2020).

Conclusion

Mobile surveying systems can produce very large data sets with hundreds of thousands of measurement points that are challenging to invert with a PC. The adaptive semi-structured finite-element mesh technique can reduce the calculation time by more than four times compared to a standard rectangular mesh for such large data sets. When combined with the segmentation method, the calculation time can be reduced by about fifteen times. Most large field surveys have noise levels of at least a few percent. Data collected using mobile surveying

systems usually have higher noise levels of above five percent. The difference in the inverse model resistivity values using a sparse adaptive semi-structured mesh from those obtained with a dense rectangular mesh is less than one percent which is much smaller than the data noise level. The use of a sparse mesh significantly reduces the calculation time with minimal effects on the final inverse model which is used for geological interpretation.

References

Aleardi, M., Vinciguerra, A. and Hojat, A. (2021) A geostatistical Markov chain Monte Carlo inversion algorithm for electrical resistivity tomography. *Near Surface Geophysics* 19, 7–26.

Barker, R.D. (1989) Depth of investigation of collinear symmetrical four-electrode arrays. *Geophysics* 54, 1031-1037.

Cherevatova, M., Egbert, G. D. and Smirnov, M. Y. (2018) A multiresolution approach to electromagnetic modelling. *Geophysical Journal International* 214(1), 656–671.

Christiansen, A.V., and Auken, E. (2004) Optimizing a layered and laterally constrained 2D inversion of resistivity data using Broyden's update and 1D derivatives. *Journal of Applied Geophysics* 56, 247-261.

Cox, L.H., Wilson, G.A. and Zhdanov, M.S. (2010) 3D inversion of airborne electromagnetic data using a moving footprint. *Exploration Geophysics* 41, 250–259.

deGroot-Hedlin, C. and Constable, S. (1990) Occam's inversion to generate smooth, two-dimensional models from magnetotelluric data. *Geophysics* 55, 1613-1624.

Davis, K. and Li, K. (2013) Efficient 3D inversion of magnetic data via octree-mesh discretization, space-filling curves, and wavelets. *Geophysics* 78, 1942-2156.

Davis, T.A. (2006) *Direct methods for sparse linear systems*. Society for Industrial and Applied Mathematics, USA.

Day-Lewis, F.D., Singha, K. and Binley, A. (2005) The application of petrophysical models to radar and electrical resistivity tomograms: resolution dependent limitations. *Journal of Geophysical Research* 110, B08206.

Demmel, J.W., S. C. Eisenstat, J. R. Gilbert, X. S. Li, and J.W. H. Liu (1999) A supernodal approach to sparse partial pivoting. *SIAM Journal on Matrix Analysis and Applications* 20, 720–755.

Devine, K, Boman, E.G. and Karypis, G. (2006) Partitioning and load balancing for emerging parallel applications and architectures. In: Heroux M, Raghavan P, Simon HD (eds) *Parallel Processing for Scientific Computing*. Society for Industrial and Applied Mathematics, USA.

Dey, A. and Morrison, H.F. (1979) Resistivity modeling for arbitrarily shaped three-dimensional shaped structures. *Geophysics* 44, 753-780.

Edwards, L.S. (1977) A modified pseudosection for resistivity and induced-polarization. *Geophysics* 42, 1020-1036.

Farquharson, C.G. and Oldenburg, D.W. (1998) Nonlinear inversion using general measures of data misfit and model structure. *Geophysical Journal International* 134, 213-227.

Farquharson, C.G. and Oldenburg, D.W. (2004) A comparison of automatic techniques for estimating the regularization parameter in non-linear inverse problems. *Geophysical Journal International* 156, 411-425.

Farquharson, C.G. (2008) Constructing piecewise-constant models in multidimensional minimum-structure inversions. *Geophysics* 73, K1-K9.

Gao, J., Smirnov, M., Smirnova, M. and Egbert, G. (2020) 3-D DC Resistivity Forward Modeling Using the Multi-resolution Grid. *Pure and Applied Geophysics* 177, 2803–2819.

George, A. and Liu, J. W-H. (1981) *Computer solution of large sparse positive definite systems*. Prentice-Hall, USA.

Günther, T., Rücker, C. and Spitzer, K. (2006) Three-dimensional modelling and inversion of dc resistivity data incorporating topography – II. Inversion. *Geophysical Journal International* 166, 506–517.

Günther, T. and Rücker, C. (2018) *Boundless Electrical Resistivity Tomography BERT 2 - the user tutorial*. Leibniz Institute for Applied Geophysics, Hannover, Germany.

Haber, E., Oldenburg, D.W. and Shekhtman R., (2007) Inversion of time domain three-dimensional electromagnetic data. *Geophysical Journal International* 171, 550–564.

Haber, E. and Heldmann, S. (2007) An OcTree Multigrid Method for Quasi-Static Maxwell's Equations with Highly Discontinuous Coefficients. *Journal of Computational Physics* 223. 783-796.

Hermann, V., Käser, M. and Castro, C.E. (2011) Non-conforming hybrid meshes for distributed non-smooth parameter identification. *Inverse Problems* 23, 1659-1576.

Holcombe, J. and Jiracek, G., (1984) 3-D terrain corrections in resistivity surveys. *Geophysics* 49, 439-452.

Inazaki, T. (2007) Integrated Geophysical Investigation for the Vulnerability Assessment of Earthen Levee. *20th EEGS Symposium on the Application of Geophysics to Engineering and Environmental Problems Proceedings*, 101-108.

Johansen, H.K. (1977) A man/computer interpretation system for resistivity soundings over horizontally stratified earth. *Geophysical Prospecting* 25, 667–691.

Kalinkin, A. and Kostin, V. (2013) *Intel Math Kernel Library (Intel MKL) Sparse Solvers*. Intel Corporation.

Kuras, O. (2002) *The Capacitive Resistivity Technique for Electrical Imaging of the Shallow Subsurface.* PhD thesis, University of Nottingham.

Kuras, O., Beamish, D., Meldrum, P.I., Ogilvy, R.D., Strange, K., Waller, M., Roberts, G.W. and Williams, G.M. (2003) Detection of abandoned mineshafts using towed-array capacitive resistivity and real-time kinematic GPS navigation. *Conference Proceedings, 9th EAGE/EEGS Meeting*, Sep 2003, Prague, cp-52-00120.

Kuras, O., Beamish D., Meldrum P.I. and Ogilvy R.D. (2006) Fundamentals of the capacitive resistivity technique. *Geophysics* 71, G135-G152.

Kuras, O., Meldrum, P.I., Beamish, D., Ogilvy, R.D. and Lala, D. (2007) Capacitive Resistivity Imaging with Towed Arrays. *Journal of Environmental & Engineering Geophysics* 12(3), 267-279.

Lelièvre, P.G. and Farquharson, C.G. (2013) Gradient and smoothness regularization operators for geophysical inversion on unstructured meshes. *Geophysical Journal International* 195, 330-341.

Loke, M.H. and Barker, R.D. (1996a) Rapid least-squares inversion of apparent resistivity pseudosections using a quasi-Newton method. *Geophysical Prospecting* 44, 131-152.

Loke, M.H. and Barker, R.D. (1996b) Practical techniques for 3D resistivity surveys and data inversion. *Geophysical Prospecting* 44, 499-523.

Loke, M.H. (2000) Topographic modelling in resistivity imaging inversion. *62nd EAGE Conference & Technical Exhibition Extended Abstracts*, D-2.

Loke, M.H. and Lane, J.W. (2004) Inversion of data from electrical resistivity imaging surveys in water-covered areas. *Exploration Geophysics* 35, 266-271.

Loke, M.H. and Dahlin, T. (2010) Methods to Reduce Banding Effects in 3-D Resistivity Inversion. *Near Surface 2010–16th European Meeting of Environmental and Engineering Geophysics*, 6 - 8 September 2010, Zurich, Switzerland, A16.

Loke M.H., Chambers J.E., Rucker D.F., Kuras O. and Wilkinson P. B. (2013) Recent developments in the direct-current geoelectrical imaging method. *Journal of Applied Geophysics* 95, 135-156.

Loke, M.H., P. B. Wilkinson, P.B., Chambers, J.E., Uhlemann, S.S. and Sorensen, J.P.R. (2015) Optimized arrays for 2-D resistivity survey lines with a large number of electrodes. *Journal of Applied Geophysics* 112, 136-146.

Loke, M.H., Wilkinson, P.B., Chambers, J. E. and Meldrum, P.I. (2018) Rapid inversion of data from 2-D resistivity surveys with electrodes displacements. *Geophysical Prospecting* 66, 579-594.

Loke, M.H., Papadopoulos, N, Wilkinson, P.B., Oikonomou, D., Simyrdanis, K. and Rucker, D.F. (2020) The inversion of data from very large 3-D ERT mobile surveys. *Geophysical Prospecting* 68, 2579-2597.

Loke, M.H., Wilkinson, P.B., Kuras, O. (2021) The use of a semi-structured finite-element mesh in 3-D resistivity inversion. *4th Asia Pacific Meeting on Near Surface Geoscience & Engineering*, Session A3: Electric, Paper Number 21, 30 November – 2 December 2021, Ho Chi Minh City, Vietnam.

Loke, M.H., Wilkinson, P.B., Gance, J., Malet, J-P., Truffert, C. and Leite, O. (2022a) Measurement and inversion strategies for 3-D resistivity surveys with vector arrays. *Geophysical Prospecting* 70, 578-592.

Loke, M.H., Wilkinson, P.B., Chambers, J.E., Uhlemann, S., Dijkstra, T. and Dahlin, T. (2022b) The use of asymmetric time constraints in 4-D ERT inversion. *Journal of Applied Geophysics* 197, 104536.

McGillivray, P.R. and Oldenburg, D.W. (1990) Methods for calculating fréchet derivatives and sensitivities for the non-linear inverse problem : a comparative study. *Geophysical Prospecting* 38, 499-524.

Maurer, H. and Friedel, S. (2006) Outer-space sensitivities in geoelectrical tomography. *Geophysics* 71, 1942-2156.

Oldenburg, D.W. and Li, Y. (2005) 5. Inversion for Applied Geophysics: A Tutorial. *Near-Surface Geophysics (SEG Investigations in Geophysics Series No. 13)*, 89-150.

Oldenburg, D.W, Haber, E. and Shekhtman, R. (2013) Three dimensional inversion of multisource time domain electromagnetic data. *Geophysics* 78, E47-E57.

Press, W.H., Teukolsky S.A., Vetterling W.T. and Flannery B.P. (2007) *Numerical Recipes in C (Third Edition)*. Cambridge University Press.

Pridmore, D.F., Hohmann, G.W., Ward, S.H. and Sill, W.R. (1981) An investigation of finite-element modeling for electrical and electromagnetic data in three dimensions. *Geophysics* 46, 1009-1024.

Rennich, S.C., Stosic, D. and Davis, T.A. (2016) Accelerating sparse Cholesky factorization on GPUs. *Parallel Computing* 59, 140-150.

Sasaki, Y. (1989) Two-dimensional joint inversion of magnetotelluric and dipole-dipole resistivity data. *Geophysics* 54, 254-262.

Schenk, O. and Gartner, K. (2002) Two-level scheduling in PARDISO: Improved Scalability on Shared Memory Multiprocessing Systems. *Parallel Computing* 28, 187-197.

Si, H. (2020) *TetGen : A Quality Tetrahedral Mesh Generator and 3D Delaunay Triangulator.* http://www.tetgen.org.

Silvester, P.P. and Ferrari R.L. (1990) *Finite elements for electrical engineers (2nd. ed.)*. Cambridge University Press.

Simyrdanis, K., Papadopoulos, N., Kim, J.H., Tsourlos, P. and Moffat, I. (2015) Archaeological Investigations in the Shallow Seawater Environment with Electrical Resistivity Tomography. *Journal of Near Surface Geophysics, Integrated geophysical Investigations for Archaeology* 13, 601- 611.

Udphuay, S., Günther, T., Everett, M.E., Warden, R.R. and Briaud, J-L. (2011) Three-dimensional resistivity tomography in extreme coastal terrain amidst dense cultural signals: application to cliff stability assessment at the historic D-Day site. *Geophysical Journal International* 185, 201–220.

Unrau, T. (2019) Towed Capacitively Coupled Resistivity Systems in Arctic Exploration - Advances in Equipment Design and Handling of Very Large Resistivity Surveys. *AGU 100 Fall Meeting*, San Francisco, 9-13 Dec. 2019, NS22A-07.

Wilkinson, P.B., Meldrum, P.I., Chambers, J.C., Kuras, O. and Ogilvy, R.D. (2006) Improved strategies for the automatic selection of optimized sets of electrical resistivity tomography measurement configurations. *Geophysical Journal International* 167, 1119-1126.

Wilkinson, P.B., Chambers, J.C., Uhlemann, S., Meldrum, P., Dixon, N. and Loke, M.H. (2016) Reconstruction of landslide movement time series by inversion of 4D electrical resistivity tomography monitoring data. *Geophysical Research Letters* 43, 1166-1174.

Xiao, L., Gianluca, F., Bo, Z., Auken, E. and Christiansen, A.V. (2022) Fast 2.5D and 3D Inversion of transient electromagnetic surveys using the octree-based finite element method. *Geophysics* 87, E267-E277.

Yang, D., Oldenburg, D.W. and Haber, E. (2014) 3-D inversion of airborne electromagnetic data parallelized and accelerated by local mesh and adaptive soundings. *Geophysical Journal International* 196, 1492–1507.

Yeralan, S.N., Davis, T.A. and Ranka, S. (2017) Algorithm 980: Sparse QR factorization on GPU architectures. *ACM Trans. on Mathematical Software* 44(12), 1-29.

Zachariadis, O., Satpute, N., Gómez-Luna, J. and Olivares, J. (2020) Accelerating sparse matrix–matrix multiplication with GPU Tensor Cores. *Computers & Electrical Engineering* 88, 106848.

Zhou, B. and Dahlin, T. (2003) Properties and effects of measurement errors on 2D resistivity imaging surveying. *Near Surface Geophysics* 1, 105-117.